Advances in Science and Technology Research Journal

Advances in Science and Technology Research Journal, 2026, 20(10), 515–526
https://doi.org/10.12913/22998624/225688
ISSN 2299-8624, License CC-BY 4.0

Received: 2026.05.20
Accepted: 2026.07.15
Published: 2026.09.01

Microstructure and wear properties of Cr_3C_2–NiCr coatings sprayed by conventional and supersonic high-velocity atmospheric plasma spraying with axial powder feeding

Tadeusz Kubaszek[1], Anita Słyś-Palacz[2], Marek Góral[1*], Marcin Drajewicz[1], Kamil Gancarczyk[1]

[1] Research and Development Laboratory for Aerospace Materials, Rzeszow University of Technology, Powstancow Warszawy 12, 35-029 Rzeszow, Poland

[2] Doctoral School of the Rzeszow University of Technology, Rzeszow University of Technology, Powstancow Warszawy 12, 35-029 Rzeszow, Poland

* Corresponding author's e-mail: mgoral@prz.edu.pl

ABSTRACT

This study investigated the microstructural evolution and phase transformation mechanisms in Cr_3C_2–NiCr cermet coatings (Metco 5241 powder) plasma-sprayed onto S235 steel substrates. Two technologies were used: conventional atmospheric plasma spraying (APS) with radial powder injection (single-electrode A60 torch) and supersonic plasma spraying with axial powder feeding (HV-APS, three-electrode Axial III torch). The HV-APS coatings exhibited nearly halved porosity (6.16% vs. 11.99% for APS) and significantly higher microhardness (1141 HV0.2 vs. 897 HV0.2). Phase analysis revealed the disappearance of primary Cr_3C_2 and $Cr_{21.26}Ni_{1.74}C_6$ carbides in favour of supersaturated Cr-Ni solid solutions. In the erosion tests conducted at a 90° impact angle, the two coating variants exhibited nearly identical specific erosion rates (0.20 mg/g for APS and 0.19 mg/g for HV-APS) and comparable damage mechanisms, dominated by fatigue-driven lamellar spalling and brittle fracture. However, in tribological tests (ball-on-disc, 30 N load), HV-APS coatings showed nearly 27% lower wear volume (2.85 mm^3) and a reduced specific wear rate (1.90×10^{-4} mm^3/Nm) compared to APS (3.90 mm^3 and 2.60×10^{-4} mm^3/Nm, respectively), correlating with their higher density and hardness. The obtained results confirm that the use of axial powder feeding in supersonic HV-APS plasma spraying significantly improves the mechanical and tribological properties of Cr_3C_2–NiCr coatings, although this advantage is not evident in the erosion tests at high impact angles.

Keywords: Cr_3C_2–NiCr, plasma spraying, HV-APS, axial feeding, microhardness, erosion, tribological wear.

INTRODUCTION

Cr_3C_2–NiCr cermet coatings are among the most widely used materials under the conditions of intense abrasive wear, erosion, and high-temperature exposure. Their performance properties are closely dependent on the used manufacturing technology, which determines the microstructure, phase composition, and number of structural defects. Among the available methods, thermal spraying techniques dominate, enabling controlled deposition while maintaining favourable carbide phase properties.

One of the most commonly used methods is high-velocity oxy-fuel (HVOF) spraying, which has become an industrial standard for producing such coatings due to its relatively low process temperature and very high particle velocities. These conditions favour the retention of a high Cr_3C_2 carbide content and limit their decarburisation and degradation [1, 2]. An alternative is the HVAF technology (High-Velocity Air-Fuel), which allows deposition at even lower temperatures, reducing oxidation and phase decomposition, thus improving, among other properties, the tribological performance of the coatings [3, 4].

Plasma spraying techniques include atmospheric plasma spraying (APS), which is widely used for the deposition of wear-resistant coatings. However, high plasma temperatures may promote carbide decomposition and the formation of metastable phases, which can adversely affect mechanical and tribological properties [5, 6]. To mitigate these effects, modified processes, such as shrouded plasma spraying (SPS) or vacuum plasma spraying (VPS) are used to reduce oxygen exposure and carbon loss during deposition [2, 7].

More advanced techniques include detonation gun spraying (D-gun), which utilises shockwave energy to produce coatings with very high density and substrate adhesion [8, 4]. Modern approaches also encompass supersonic atmospheric plasma spraying (SAPS), compact plasma spraying (CPS) systems, and hybrid technologies, including laser-assisted processes [9, 10, 11]. Of particular interest in recent years is supersonic plasma spraying (SAPS), which combines very high plasma temperatures (up to 20,000 K) with supersonic particle velocities (in range 300–800 m/s). This process employs other types of torches (e.g., HEPJet-II, SG-100) equipped with de Laval nozzles, which allow for achieving high kinetic energy with relatively low gas consumption [12, 13]. The coatings produced using this method feature a dense lamellar structure and low porosity (1.1–4.3%), and high hardness (often exceeding 1000 HV), attributed to the presence of supersaturated solid solutions and metastable phases [2, 14]. The designs utilising cascade anodes and multi-cathode configurations (e.g., Sinplex, Triplex Pro-210, Oerlikon-Metco) stabilise the electric arc and minimise voltage fluctuations [15]. Such process stability drastically limits the decarburisation of carbides and their oxidation during in-flight, thereby preserving the original crystallographic structure of the feedstock material ([15,16] Furthermore, the application of high-efficiency supersonic (HEPJet) torches operating in an inert atmosphere reduces the exposure time of particles to extreme temperatures [17]. This results in minimised carbon loss and a significant increase in deposition efficiency (up to 54%), while maintaining high coating hardness (approx. 884 HV0.3) and excellent adhesion to the substrate [17]. Owing to these solutions, it is possible to produce coatings with a dense, homogeneous microstructure that exhibit outstanding wear resistance [17,15]. An important direction in the development of plasma technologies is the application of axial powder feeding, which ensures more efficient particle heating and better acceleration within the plasma plume. Compared to conventional radial feeding in plasma torches, this allows for a significant reduction in porosity and an increase in coating hardness [17]. Comparative analyses indicate that the properties of Cr_3C_2–NiCr coatings strongly depend on the used technology. The coatings produced by HVAF exhibit higher hardness and better wear resistance than HVOF [3], while SAPS can provide lower porosity and higher deposition efficiency [12]. Methods such as VPS or reactive plasma spraying (RPS) enable specific mechanical and tribological properties, including high fracture toughness and wear resistance [7, 18, 19]. Consequently, the appropriate selection of thermal spraying technology is a key factor in designing Cr_3C_2–NiCr coatings, determining their microstructure, mechanical properties, and operational durability under demanding conditions. To further explore these dependencies, the objective of this study was to analyse the relationship between the powder injection method (axial vs. radial) and the resulting phase evolution and wear behaviour of such coatings. The research focused on evaluating how the higher energy of the HV-APS process affects the degree of carbide dissolution and how these structural transformations influence the performance of the coating under sliding and erosion conditions. This work, conducted as a continuation of previous studies [19,20,21], provides a comparative analysis of coatings produced by an Axial III torch with axial feeding and a conventional A60 torch with radial injection.

MATERIALS AND METHODS

S235 carbon steel was used as substrate material, from which specimens in the form of 4mm thick plates were prepared. Before spraying, the samples underwent standard pre-treatment, comprising cleaning and degreasing of the surface to ensure adequate coating adhesion, preceded by sandblasting using 40-grit electrocorundum.

Cr_3C_2–NiCr coatings were deposited using Metco 5241 powder (Oerlikon Metco, USA), a gas-atomised and blended cermet feedstock. According to the manufacturer's technical data, the powder has a nominal chemical composition of approximately 58.5 wt.% Cr, 34 wt.% Ni, and 7.5 wt.% C. As shown in Figure 1a,b the feedstock powder consists of predominantly spherical particles with a gas-atomised morphology. High-magnification SEM observations reveal an internal agglomerated and partially sintered structure with a fine distribution of carbide phases. These characteristics ensure stable powder feeding and uniform injection during thermal spraying. Particle size distribution (PSD) analysis (Figure 1c) is consistent with the nominal −45 +15 μm fraction, with characteristic diameters of D10 = 10.01 μm, D50 = 19.73 μm, and D90 = 32.81 μm. Although this type of Cr_3C_2–NiCr powder is primarily developed for HVOF spraying, it was used in the present study for comparative evaluation of conventional APS (A60) and HV-APS (Axial III) processes with respect to phase stability and microstructural evolution.

The spraying processes were carried out using a Thermico GmbH (Dortmund, Germany). system equipped with two types of plasma torches: a three-electrode torch with axial powder feeding, type Axial III (HV-APS), and a conventional single-electrode torch, type A60 (APS). The spraying process involved the use of a Fanuc M710iC industrial robot (Fanuc Corporation, Oshino, Japan) for torch manipulation, while compressed air cooling was used to maintain stable thermal conditions for the substrate during coating formation. The process parameters were selected based on previous experimental studies [20, 21] and are summarised in Table 1.

Microstructural characterisation of the coatings was performed using a Phenom XL scanning electron microscope (SEM) (Thermo Fisher Scientific, Waltham, MA, USA) equipped with an energy-dispersive X-ray spectroscopy (EDS) system. The average coating thickness was evaluated on the basis of SEM micrographs at a magnification of 320x. For each variant, 40 individual measurements were taken (10 points across 4 representative cross-sections) to ensure statistical

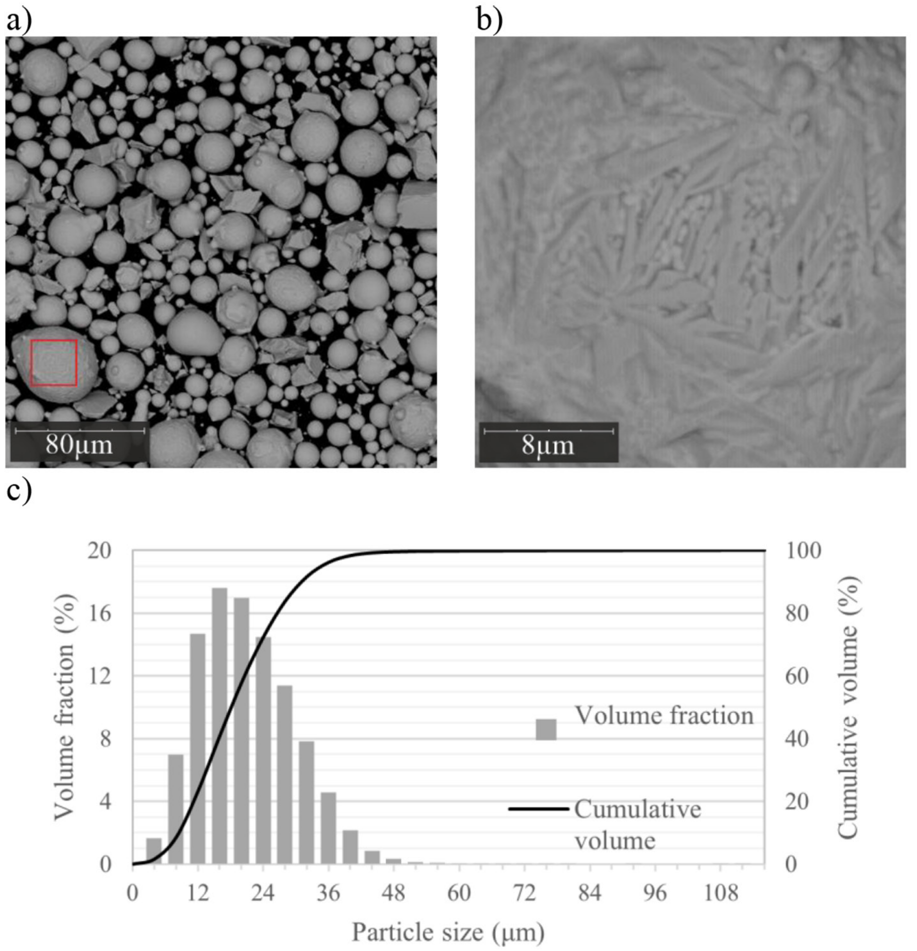

Figure 1. Characteristics of the Metco 5241 (Cr_3C_2–NiCr) feedstock powder: (a) SEM micrograph showing the morphology of the particles at 1000x magnification; (b) high-magnification SEM image (10000x) of the area marked with a red frame in (a), revealing the surface details of the agglomerated structure; (c) particle size distribution (PSD) presented as incremental volume fraction (bars) and cumulative volume (line)

Table 1. Plasma spraying parameters for HV-APS and APS

Process parameter	A60 (APS)	Axial III (HV-APS)
Spray distance [mm]	100	100
Powder feed rate [g/min]	25	25
Current [A]	450	480*
Number of torch passes [-]	60	60
Deposition rate [µm/pass]	7.69	9.19
Torch traverse speed [mm/s]	1000	1000
Argon flow rate [NLPM]	68	140
Hydrogen flow rate [NLPM]	5	20
Nitrogen flow rate [NLPM]	–	100

Note: *Total current for the three-electrode Axial III torch (160 A per electrode)

reliability. Furthermore, the deposition rate [µm/pass] was determined by dividing the total average thickness by the number of torch passes (60). The coating porosity was determined by image analysis based on SEM micrographs at a magnification of 2000x, using the Leica Application Suite v3.7 software. Measurements were taken from ten different cross-sectional areas of each sample, and then the average porosity value was calculated.

The particle size distribution (PSD) of the Metco 5241 powder was measured using an IPS U analyser (Kamika Instruments, Poland). The analysis was performed using an infrared diode light source and 256 size classes. Each measurement was repeated three times and the final results were reported as the average value.

The surface roughness of all samples was measured using a Surftest SJ-210 (Mitutoyo, Kawasaki, Japan) equipped with SJ-Communication-Tool software, in accordance with the ISO 21920-2:2021 standard. For each coating variant, ten measurements were performed to determine the mean values and standard deviations of the Ra parameter. Measurements were conducted both after the sandblasting process to characterise the substrate preparation and on the surface of the as-sprayed coatings.

X-ray diffraction (XRD) analysis of the feedstock powder and the APS (A60) and HV-APS (Axial III) coatings was performed using an ARL X'Tra diffractometer (Thermo Fisher Scientific, USA). The diffraction patterns were recorded in the 2θ range of 20°–80° using Bragg–Brentano geometry with CuKα radiation (λ = 0.1540562 nm). Measurements were carried out with a step size of 0.02°/3s. Phase identification was performed by matching the diffraction patterns with the ICDD PDF database.

Microhardness measurements were carried out using a Nexus 4303 (Innovatest, The Netherlands) microhardness tester according to the Vickers method. A load corresponding to the HV0.2 scale (0.2 kgf ≈ 1.96 N) was applied, with a dwell time of 10 s. The obtained hardness values are reported as HV0.2. To ensure statistical reliability and account for the structural heterogeneity of the cermet coatings, twenty indentations were made on the cross-section of each coating variant, and the results are presented as mean values.

Erosion resistance tests were conducted in accordance with the ASTM G73 standard, using a TR-470 (Koehler Instrument Company, USA) apparatus at room temperature (25 °C). Specimens of 25 × 25 mm in dimensions were subjected to an abrasive particle stream for 10 minutes. The erodent feed rate was 2 g/min, at an air pressure of 0.2 kg/cm². The test was carried out at an impact angle of 90°. The mass loss was determined based on the measurements taken before and after the test using a KERN ABT 120-4M analytical balance (KERN & SOHN GmbH, Germany) with an accuracy of 1×10^{-4} g. The results were expressed as the specific erosion rate (E) in mg/g, calculated as the mass loss per unit mass of erodent (20 g total). The morphology of the erosion craters was characterised using SEM at a magnification of 4000x in BSE mode.

The tribological properties were evaluated using the ball-on-disc method with a T-01M tribotester (Łukasiewicz Research Network – ITeE, Poland), following the ASTM G99-17 standard. The adopted parameters included a linear speed of 0.1 m/s, a load of 30 N, and a sliding distance of 500 m. A tungsten carbide ball (WC) with a diameter of 10 mm and a hardness of 1741±5 HV10 was used as a counterbody. The choice of the tungsten carbide (WC) ball was driven by the need to preserve the complete comparability of results within a larger and ongoing research programme focused on different cermet coatings deposited using A60 and Axial III torches. This approach maintains consistency in the experimental setup and enables a reliable assessment of how torch configuration affects the wear mechanisms of various coating types. The volume loss of the disc was calculated using the formula specified in ASTM G99:

$$Disk\ volume\ loss = 2\pi R\left[r^2 sin^{-1}\left(\frac{d}{2r}\right) - \left(\frac{d}{4}\right)(4r^2 - d^2)^{\frac{1}{2}}\right] \quad (1)$$

where: r is the radius of the ball [mm], R is the radius of the wear track [mm] and d is the width of the wear track [mm].

The width of the wear track (d) was determined using a Leica DMI3000 M optical microscope (Leica Microsystems, Germany) operated in bright-field mode at 5× magnification. For each wear track, four randomly chosen areas were evaluated and five separate width measurements were taken per image, yielding a total of 20 measurements for each type of coating with the Leica Application Suite v3.7 software. The mean values of d were then used to calculate the material volume loss (V_{loss}). After tribological tests, the wear tracks were examined using SEM to determine the dominant wear mechanisms. SEM imaging was carried out at 320× and 1000× magnification in the BSE mode. The wear resistance was assessed in terms of material Vloss and further represented as a specific wear rate (k), which normalises volume loss by applied load and overall sliding distance, allowing a standardised comparison among the different coating variants. The specific wear rate is defined as:

$$k = \frac{V_{loss}}{F \cdot s} \quad (2)$$

where: k is the specific wear rate, [$mm^3 \cdot N^{-1} \cdot m^{-1}$], V_{loss} is the material volume loss [mm^3], F is the applied normal load [N] and s is the sliding distance [m].

RESULTS AND DISCUSSION

Microstructure and porosity

The Cr_3C_2-NiCr coatings produced with both the single-electrode A60 torch and the three-electrode Axial III torch exhibit a lamellar structure typical of the APS method with visible splat boundaries and pores (Figure 2a,b). The average coating thickness was 461.12 ±12.40 µm for the APS coating and 551.28 ±11.76 µm for the HV-APS coating (Figure 3). Although both coatings were deposited using the same number of passes (60), robot traverse speed (1000 mm/s), and powder feed rate, the HV-APS coating was approximately 19.5% thicker. This increase reflects the higher deposition efficiency of the Axial III torch, corresponding to a deposition rate of 9.19 µm/pass compared with 7.69 µm/pass for the conventional A60 system (Table 1).

Porosity measurements revealed that the use of the Axial III torch yielded the coatings with an average porosity of 6.16 ± 0.69 vol.%, which is nearly half the value of the coating sprayed with the conventional single-electrode A60 torch (11.99 ± 1.73 vol.%). This result correlates with the observations by Xie et al. [17], who indicated that axial feeding provides optimal heat transfer and higher in-flight particle kinetic energy. The higher degree of particle flattening upon impact with the substrate leads to a denser, more sealed structure. However, it should be noted that these coatings exhibit higher porosity than those produced by the HVOF methods, where porosity often falls below 2% [5, 22], or supersonic plasma spraying (SAPS), which can achieve porosity levels of around 1.31% [12].

The surface state of the samples was also evaluated in key stages of the process. The average roughness of the substrate after sandblasting was Ra=3.02±0.20 µm. Following the deposition process, the surface roughness increased significantly for both variants, reaching 8.35±0.69 µm for the APS coating and 8.34±0.80 µm for the HV-APS variant. The lack of significant differences in Ra values between the two plasma torches suggests that at the final stage of coating formation, the surface topography is governed primarily by the particle size distribution of the feedstock powder (-45 +15 µm) and the overlap of individual splats, rather than the kinematics of the torch or the velocity of the particles.

Qualitative chemical characterisation was performed using EDS elemental mapping (Figure 4) to evaluate the distribution of Ni, Cr, and O within the coating microstructure. Nickel, constituting the matrix phase, exhibits a relatively uniform distribution throughout the analysed regions. Chromium is enriched in localised regions, while also being distributed within the Ni-rich matrix, suggesting partial dissolution of the carbide phase during plasma spraying, as confirmed by the subsequent XRD analysis. Oxygen is mainly localised along the lamellar boundaries and in the vicinity of pores, indicating the localised oxide formation resulting from high-temperature exposure during the spraying process.

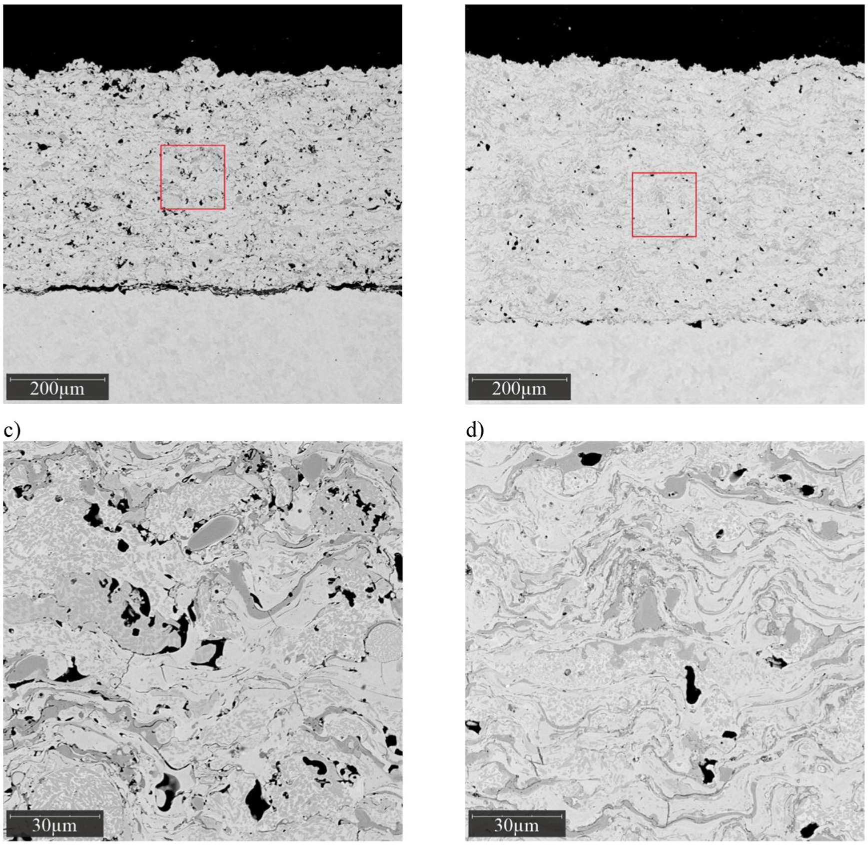

Figure 2. SEM cross-sectional micrographs of the Cr_3C_2–NiCr coatings: (a) overview of the APS (A60) coating (320× magnification); (b) overview of the HV-APS (Axial III) coating (320× magnification); (c) high-magnification view (2000×) of the area marked with a red frame in (a); (d) high-magnification view (2000×) of the area marked with a red frame in (b)

XRD phase analysis results (Figure 5) indicate significant phase transformations in the plasma-sprayed coatings compared to the feedstock material. In line 1 (Metco 5241 powder), distinct, sharp peaks corresponding to Cr_3C_2 and $Cr_{21.26}Ni_{1.74}C_6$ carbide phases are visible. The produced coatings (lines 2 and 3) show a significant reduction in the intensity of carbide peaks together with the appearance of diffraction peaks corresponding to Cr–Ni solid solution phases, such as $Cr_{0.8}Ni_{0.2}$ and $Cr_{0.114}Ni_{0.886}$. This phenomenon is consistent with extensive carbide dissolution into the NiCr matrix under the high thermal energy of the plasma arc, and is widely described in the literature as typical for high-enthalpy processes [2, 10]. As indicated by Rubino et al. [10], substantial dissolution of the primary carbide leads to the formation of supersaturated solid solutions, which Matthews [2] defined as a key mechanism of structural changes during theee plasma spraying of cermet coatings.

The comparison of the diffractograms of the coatings obtained with both torches is particularly significant. It can be observed that the metallic phase peaks for the coating obtained with the Axial III torch (line 2) are distinctly broader and

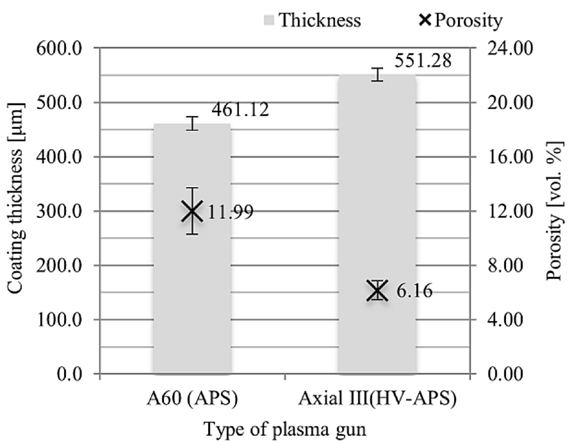

Figure 3. Average thickness and porosity of Cr_3C_2-NiCr coatings sprayed by conventional APS (A60 torch) and HV-APS (Axial III torch)

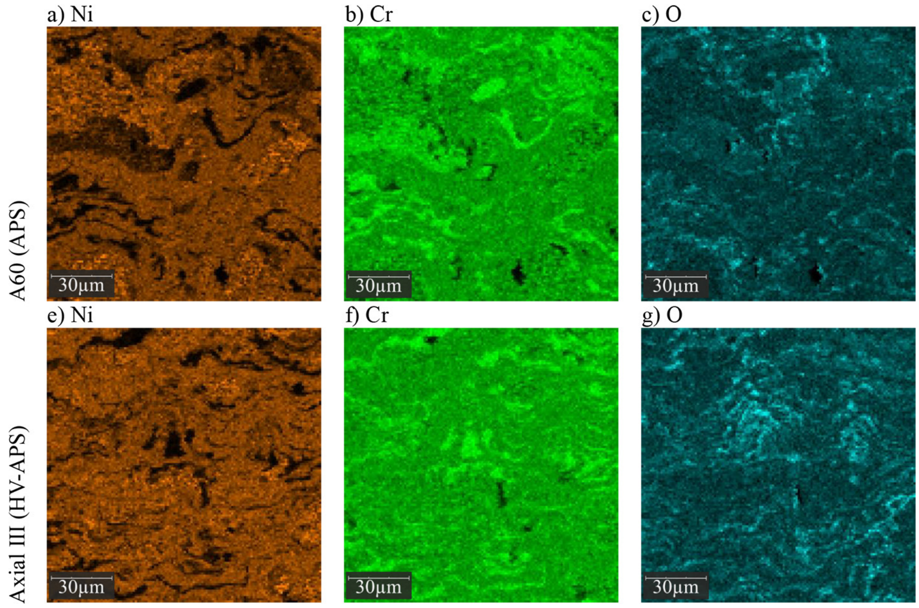

Figure 4. EDS elemental mapping of the Cr_3C_2-NiCr coatings obtained from the areas shown in Figure 2c and Figure 2d: (a–c) distribution of Ni, Cr, and O for the APS (A60) coating; (d–f) distribution of Ni, Cr, and O for the HV-APS (Axial III) coating variant

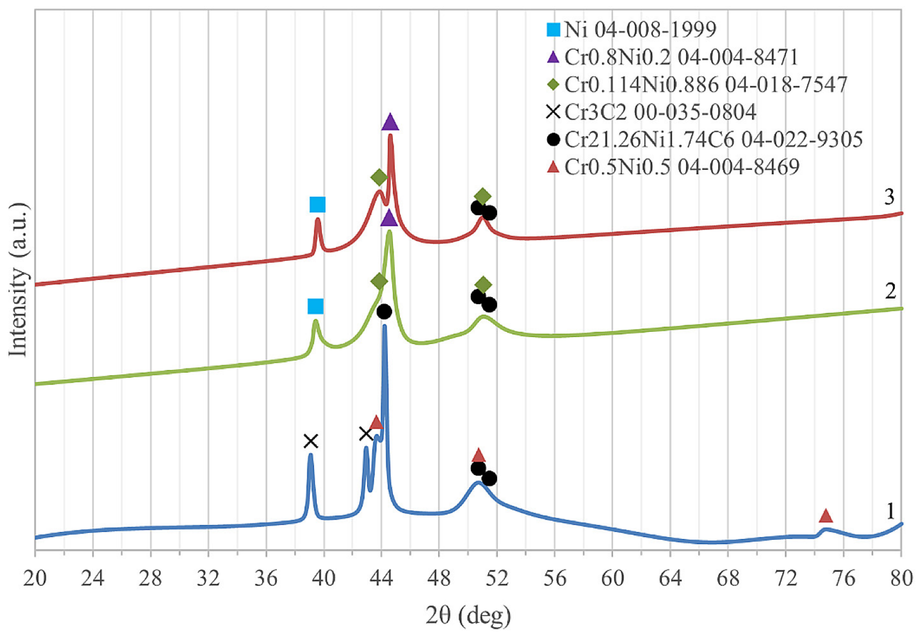

Figure 5. Diffractograms of the Metco 5241 powder (1) and the carbide coating produced from Metco 5241 powder using: 2 – Axial III torch and 3 – A60 torch

more diffuse compared to the coating produced with the A60 torch (line 3). Such peak broadening may indicate the formation of a nanocrystalline structure due to extremely high splat cooling rates on the order of 10^6–10^8 K/s, or even partial amorphisation [14, 10]. However, these observations remain qualitative, and confirmation of crystallite size or amorphous content would require complementary characterisation techniques, such as TEM, while reliable quantitative phase analysis would require Rietveld refinement. These results are close to the conclusions of Alroy et al. [4], who reported a significant degree of phase decomposition and minimal carbide retention for axial injection systems. In contrast, the studies on HVOF technology by Zhang et al. [5] demonstrated a much better retention of primary Cr_3C_2 due to lower flame temperatures. Although the intensive carbide dissolution visible in the diffractograms (Figure 5) promotes high hardness through solid-solution and dispersion strengthening of the matrix [3, 21], as noted by Liu et al. [9], it may lead to increased chromium oxidation in the plasma jet and the formation of secondary phases, such as metastable $(Cr,Ni)_7C_3$ [14].

Coating hardness

The average hardness of the Cr_3C_2-NiCr coating obtained with the three-electrode Axial III torch was 1141±91 HV0.2, which is significantly higher compared to the coating sprayed with the single-electrode A60 plasma torch 897±123 HV0.2 (Figure 6). The hardness value obtained for the Axial III torch coating is higher than those achieved by supersonic plasma spraying (SPS), for which Zhang et al. [5] and Lin et al. [12] reported values around 821 HV, and also higher than HVOF-sprayed coatings, where hardness rarely exceeds 900 HV [8, 5]. Comparable hardness values to the Axial III torch coating were only obtained by Mahade et al. [3] using the HVAF process (approx. 1091 HV). The achievement of such high hardness in the present study is directly related to the characteristics of the Axial III torch. The high enthalpy of the plasma jet promotes intensive dissolution of the carbide phase and supersaturation of the metallic matrix with carbide-forming elements, leading to strong solid solution strengthening, confirmed by the disappearance of crystalline phases in favour of hard solid solutions. Additionally, the higher hardness in the Axial III system correlates with porosity reduction to 6.16% (compared to 11.99% for the A60 torch), which, according to studies by Xie et al. [17], is crucial for increasing the cohesion of the lamellar structure and resistance to indenter penetration.

Erosion resistance

Erosion resistance tests at an impact angle of 90° showed similar specific erosion rates (Figure 7) for the coatings produced with the single-electrode A60 torch (0.20 mg/g) and the three-electrode Axial III torch (0.19 mg/g). At high erodent impact angles, the damage mechanism transforms from micro-cutting and grooving to fatigue-induced spalling of entire lamellae, where resistance is determined not merely by pore volume, but by the hardness of individual phase constituents and the quality of interlamellar bonding [5]. SEM observations of the erosion craters at a magnification of 4000x (Figure 8) provide direct evidence of these phenomena. For both the APS (Figure 8a) and HV-APS (Figure 8b) variants, the surface is characterised by extensive brittle fragmentation and multi-directional microcracks propagating along interlamellar boundaries. According to Xie et al. [17] and Liu et al. [23] improving interlamellar bonding and increasing hardness are crucial for hindering the propagation of vertical and subsurface cracks, which are the main cause of cermet

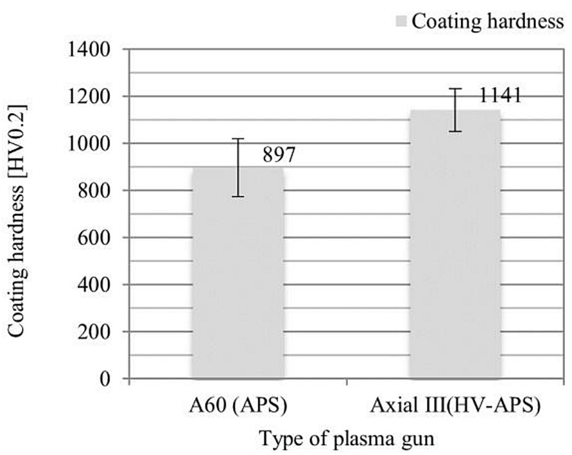

Figure 6. Microhardness of Cr_3C_2-NiCr coatings sprayed by conventional APS (A60 torch) (a) and HV-APS (Axial III torch) (b)

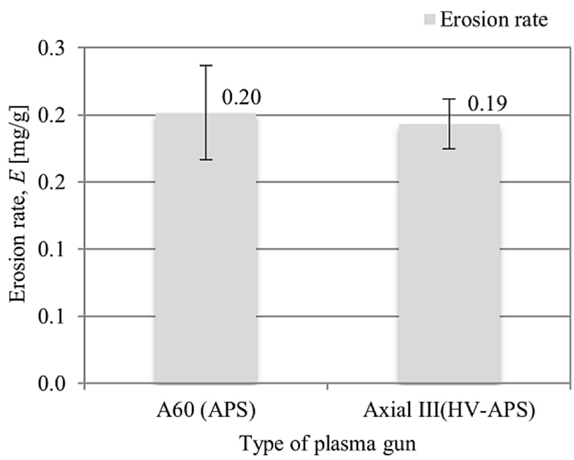

Figure 7. Specific erosion rate of Cr_3C_2-NiCr coatings sprayed by conventional APS (A60 torch) and HV-APS (Axial III torch)

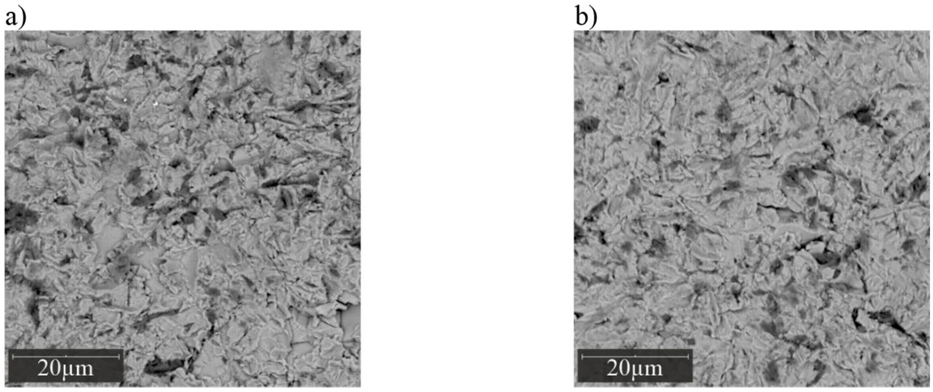

Figure 8. SEM micrographs of the erosion craters after testing at a 90° impact angle at 4000x magnification: (a) APS A60 coating; (b) HV-APS Axial III coating

degradation at high impact angles [6]. The similar performance of both coatings at 90° suggests that the interlamellar cohesion reached a comparable threshold for both plasma technologies. This is further supported by literature data [5] which indicate that maximum erosion rates occur at angles in the range of 60°–75°, and the advantage of high-velocity systems (HVOF/HVAF), which provide superior erosion resistance through drastic microstructure densification, becomes more apparent under those conditions.

Tribological wear resistance

Ball-on-disc tribological tests demonstrated better wear resistance for the Cr_3C_2-NiCr coating produced by the HV-APS method compared to the coating by the conventional APS plasma spray process. Based on the analysis of SEM micrographs of the wear tracks (Figure 9) and volume loss (V_{loss}) and specific wear rate (k) calculations (Figure 10), the coating obtained with the Axial III torch (HV-APS) was 2.85 mm^3, which is approximately 27% lower than that for the

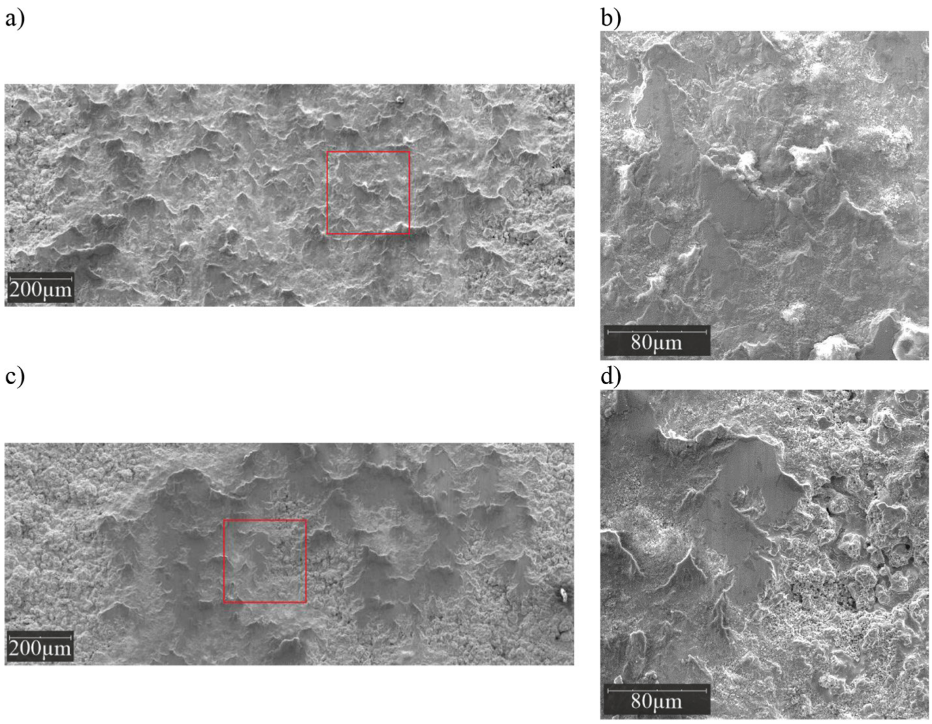

Figure 9. SEM micrographs of wear tracks for Cr_3C_2-NiCr coatings: (a, b) APS A60 and (c, d) HV-APS Axial III. Overviews at 320x (a, c) and 1000x details (b, d) of the areas marked with red frames

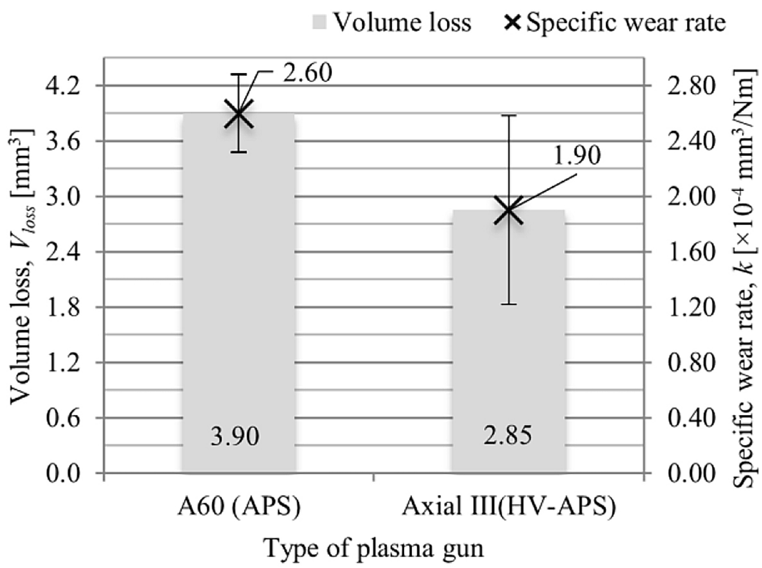

Figure 10. Average volume loss (Vloss) and specific wear rate (k) of Cr_3C_2-NiCr coatings sprayed by conventional APS (A60 torch) and HV-APS (Axial III torch) after the ball-on-disc wear test (load 30 N, sliding distance 500 m)

coating sprayed with the A60 torch (3.90 mm³). To provide a standardised measure, the results were also converted to the specific wear rate (*k*). The HV-APS coating exhibited a wear rate of 1.90 ±0.68 × 10^{-4} mm^3/Nm, compared to 2.60 ±0.28 × 10^{-4} mm^3/Nm for the APS coating. The higher resistance of the coating obtained with the Axial III torch is attributed to its lower porosity (6.16%) and higher average hardness (1141 HV0.2). In contrast, the higher porosity of the A60 torch coating (11.99%) promoted micro-damage initiation and accelerated material degradation under the 30 N load through micro-cutting and lamellar spalling mechanisms clearly visible as fragmented areas in Figure 9 a, b. In contrast, the HV-APS coating showed a more cohesive and smoother wear surface (Figure 9c, d), confirming that lower porosity effectively limits material removal.

These results find some confirmation in the publication by Xie et al. [17], who showed that axial powder feeding (a system analogous to Axial III) allows obtaining coatings with a wear coefficient lower almost by a factor of ten compared to radial feeding, due to better particle melting and a denser structure. Similar dependencies are reported by Lin et al. [12], indicating that in supersonic plasma spraying (SPS) systems, the mass loss is lower than in the coatings with a higher number of structural defects. Mahade et al. [3] and Liu et al. [23] emphasised that the tribological resistance of cermets is closely correlated with the hardness of the matrix and the degree of hard phase retention. The high hardness of the coating obtained in the HV-APS Axial III process (comparable to the HVAF technology reported by Mahade [3]) became a key factor limiting the penetration of the WC indenter.

CONCLUSIONS

The use of supersonic plasma spraying with axial powder feeding (HV-APS, Axial III torch) allows obtaining the Cr_3C_2–NiCr coatings with nearly halved porosity (6.16%) compared to conventional APS (11.99%).

In both technologies, the primary Cr_3C_2 carbides decompose into supersaturated Cr–Ni solid solutions. However, the broader diffraction peaks observed for the HV-APS coating may indicate a finer nanocrystalline structure and/or increased lattice distortion compared to the A60 coating.

HV-APS coatings achieve significantly higher microhardness (1141 HV0.2) than APS coatings (897 HV0.2), which is comparable to the results reported for the advanced HVAF technology.

In erosion tests at a 90° impact angle, no significant differences in erosion rate were found (0.20 mg/g for APS vs 0.19 mg/g for HV-APS). SEM analysis of the erosion craters confirmed that the dominant mechanism is fatigue-induced lamellar spalling, which, under these specific conditions, is more dependent on interlamellar bonding quality than on global porosity or microhardness.

In tribological tests (ball-on-disc, 30 N), the HV-APS coatings were approximately 27% lower wear volume (2.85 mm^3) and a lower specific wear rate (1.90 ±0.68 × 10-4 mm^3/Nm) compared to the APS coatings (3.90 mm^3 and 2.60 ±0.28 × 10-4 mm^3/Nm, respectively). The SEM analysis of the wear tracks confirmed that improved performance is due to a shift in the wear mechanism: from extensive lamellar spalling and fragmentation in the APS variant to a more controlled abrasive wear in the denser and harder HV-APS coatings.

REFERENCES

1. Shukla V.N., Jayaganthan R., Tewari V.K. Degradation behavior of HVOF-sprayed Cr_3C_2–25%NiCr cermet coatings exposed to high temperature environment. Mater. Today Proc. 2015;2(4–5):1805–1813. https://doi.org/10.1016/j.matpr.2015.07.048
2. Prudenziati M., Gazzadi G.C., Medici M., Dalbagni G., Caliari M. Cr_3C_2–NiCr HVOF-sprayed coatings: microstructure and properties versus powder characteristics and process parameters. J. Therm. Spray Technol. 2010;19:541–550. https://doi.org/10.1007/s11666-009-9458-3
3. Mahade S., Mulone A., Björklund S., Klement U., Joshi S. Investigating load-dependent wear behavior and degradation mechanisms in Cr_3C_2–NiCr coatings deposited by HVAF and HVOF. J. Mater. Res. Technol. 2021;15:4595–4609. https://doi.org/10.1016/j.jmrt.2021.10.088
4. Alroy R.J., Kamaraj M., Lakshmi D.V., Praveen K., Suresh Babu P., Sivakumar G. Tailoring microstructural features of Cr_3C_2–25NiCr coatings through diverse spray variants and understanding the high-temperature erosion behavior. Tribol. Int. 2023;188:108810. https://doi.org/10.1016/j.triboint.2023.108810
5. Zhang X., Li F., Li Y., Lu Q., Li Z., Lu H., Ran X., Qi X. Comparison on multi-angle erosion behavior and mechanism of Cr_3C_2–NiCr coatings sprayed by SPS and HVOF. Surf. Coat. Technol. 2020;403:126366. https://doi.org/10.1016/j.surfcoat.2020.126366
6. Lu H., Shang J., Jia X., Li Y., Li F., Li J., Nie Y. Erosion and corrosion behavior of shrouded plasma sprayed Cr_3C_2–NiCr coating. Surf. Coat. Technol. 2020;388:125534. https://doi.org/10.1016/j.surfcoat.2020.125534
7. Marcano Z., Lesage J., Chicot D., Mesmacque G., Puchi-Cabrera E.S., Staia M.H. Microstructure and adhesion of Cr_3C_2–NiCr vacuum plasma sprayed coatings. Surf. Coat. Technol. 2008;202(18):4406–4410. https://doi.org/10.1016/j.surfcoat.2008.04.017
8. Aditya Y.N., Venkata Ramana P., Akshay Y., Ramanjaneyulu K. Investigation of detonation spray deposited Cr_3C_2-NiCr cermet coatings for hard-facing applications. Mater. Today Proc. 2023. https://doi.org/10.1016/j.matpr.2023.02.075
9. Liu Q., Wang Y., Bai Y., Li Z.D., Tan G.L., Bao M.Y., Li X.J., Zhan H., Sun Y.W., Chong N.J., Wang R.J., Ma Y.S. Formation mechanism of gas phase in supersonic atmospheric plasma sprayed NiCr-Cr_3C_2 cermet coatings. Surf. Coat. Technol. 2020;397:126052. https://doi.org/10.1016/j.surfcoat.2020.126052
10. Rubino F., Merino D., Silvestri A.T., Munez C., Poza P. Mechanical properties optimization of Cr_3C_2-NiCr coatings produced by compact plasma spray process. Surf. Coat. Technol. 2023;465:129570. https://doi.org/10.1016/j.surfcoat.2023.129570
11. hLin L., Li G.-L., Wang H.-D., Kang J.-J., Xu Z.-L., Wang H.-J. Structure and wear behavior of NiCr-Cr_3C_2 coatings sprayed by supersonic plasma spraying and high velocity oxy-fuel technologies. Appl. Surf. Sci. 2015;356:383–390. https://doi.org/10.1016/j.apsusc.2015.08.019
12. Zhang Y., Chong K., Liu Q., Bai Y., Zhang Z., Wu D., Zou Y. High-temperature tribological behavior of thermally-treated supersonic plasma sprayed Cr_3C_2-NiCr coatings. Int. J. Refract. Met. Hard Mater. 2021;95:105456. https://doi.org/10.1016/j.ijrmhm.2020.105456
13. Matthews S. Compositional development as a function of spray distance in unshrouded/shrouded plasma-sprayed Cr_3C_2-NiCr coatings. J. Therm. Spray Technol. 2015;24(3):515–533. https://doi.org/10.1007/s11666-014-0212-0
14. Mulpuri N., Dzhurinskiy D., Dautov S., Babu A., Yakimchuk A. Structure and electrochemical behavior of coatings from complex concentrated alloys deposited by Metco Triplex Pro-210 gun. Mater. Today Proc. 2023. https://doi.org/10.1016/j.matpr.2023.11.107
15. Manojkumar P., Kalyani B., Vijaya Lakshmi D., Rama Krishna L., Sivakumar G. Realizing wear-resistant Cr_2O_3 coatings using finer feedstock: role of diverse plasma spray torch configurations. Ceram. Int. 2025;51(18B):25960–25967. https://doi.org/10.1016/j.ceramint.2025.03.279
16. Xie J., Fang H., Wang Y., Wang W., Yu J., Li J., He X., Pu J. Controlling the porosity to enhance the high-temperature tribological performance of plasma-sprayed NiCr– Cr_3C_2–BaF_2/CaF_2 coating by adopting axial feeding. J. Mater. Res. Technol. 2025;36:2577–2588. https://doi.org/10.1016/j.jmrt.2025.03.273
17. Staia M.H., Valente T., Bartuli C., Lewis D.B., Constable C.P., Roman A., Lesage J., Chicot D., Mesmacque G. Part II: tribological performance of Cr_3C_2-25%NiCr reactive plasma sprayed coatings deposited at different pressures. Surf. Coat. Technol. 2001;146–147:563–570. https://doi.org/10.1016/S0257-8972(01)01438-4
18. Kubaszek T., Kościelniak B., Góral M., Głód W. The influence of plasma spraying process parameters

on microstructure and selected properties of novel NiCrAl- Cr_3C_2 composite coating. Solid State Phenomena 2026;385:37–44. https://doi.org/10.4028/p-8PdEdl

19. Góral M., Kubaszek T., Graboń W.A., Grochalski K., Drajewicz M. The concept of WC-CrC-Ni plasma-sprayed coating with the addition of YSZ nanopowder for cylinder liner applications. Materials 2023;16(3):1199. https://doi.org/10.3390/ma16031199
20. Kubaszek T., Góral M., Słyś A., Szczęch D., Gancarczyk K., Drajewicz M. The influence of HV-APS process parameters on microstructure and erosion resistance of metalloceramic WC-CrC-Ni coatings. Ceram. Int. 2023;49(11A):18007–18013. https://doi.org/10.1016/j.ceramint.2023.02.148
21. Wang H., Li H., Zhu H., Cheng F., Wang D., Li Z. A comparative study of plasma sprayed TiB2–NiCr and Cr_3C_2–NiCr composite coatings. Mater. Lett. 2015;153:110–113. https://doi.org/10.1016/j.matlet.2015.04.015
22. Liu S., Wu H., Xie S., Yu Z., Luo H., Yazdi M.A.P., Planche M.-P., Molière M., Liao H. Effect of stoichiometry conditions on the erosion and sliding wear behaviors of Cr_3C_2–NiCr coatings deposited by a novel ethanol-fueled HVOF process. Surf. Coat. Technol. 2023;454:129084. https://doi.org/10.1016/j.surfcoat.2022.129084